

# High-performance piezoelectric composites via $\beta$ phase programming

Received: 9 April 2022

Accepted: 3 August 2022

Published online: 18 August 2022

Check for updates

Yuanjie Su<sup>1,6</sup>, Weixiong Li<sup>1,6</sup>, Xiaoxing Cheng<sup>2,6</sup>, Yihao Zhou<sup>3,6</sup>, Shuai Yang<sup>4</sup>, Xu Zhang<sup>5</sup>, Chunxu Chen<sup>1</sup>, Tiannan Yang<sup>2</sup>✉, Hong Pan<sup>1</sup>, Guangzhong Xie<sup>1</sup>, Guorui Chen<sup>3</sup>, Xun Zhao<sup>3</sup>, Xiao Xiao<sup>3</sup>, Bei Li<sup>5</sup>✉, Huiling Tai<sup>1</sup>, Yadong Jiang<sup>1</sup>, Long-Qing Chen<sup>2</sup>, Fei Li<sup>4</sup>✉ & Jun Chen<sup>3</sup>✉

Polymer-ceramic piezoelectric composites, combining high piezoelectricity and mechanical flexibility, have attracted increasing interest in both academia and industry. However, their piezoelectric activity is largely limited by intrinsically low crystallinity and weak spontaneous polarization. Here, we propose a  $\text{Ti}_3\text{C}_2\text{T}_x$  MXene anchoring method to manipulate the intermolecular interactions within the all-*trans* conformation of a polymer matrix. Employing phase-field simulation and molecular dynamics calculations, we show that OH surface terminations on the  $\text{Ti}_3\text{C}_2\text{T}_x$  nanosheets offer hydrogen bonding with the fluoropolymer matrix, leading to dipole alignment and enhanced net spontaneous polarization of the polymer-ceramic composites. We then translated this interfacial bonding strategy into electrospinning to boost the piezoelectric response of samarium doped Pb ( $\text{Mg}_{1/3}\text{Nb}_{2/3}$ ) $\text{O}_3$ - $\text{PbTiO}_3$ /polyvinylidene fluoride composite nanofibers by 160% via  $\text{Ti}_3\text{C}_2\text{T}_x$  nanosheets inclusion. With excellent piezoelectric and mechanical attributes, the as-electrospun piezoelectric nanofibers can be easily integrated into the conventional shoe insoles to form a foot sensor network for all-around gait patterns monitoring, walking habits identification and Metatarsalgi prognosis. This work utilizes the interfacial coupling mechanism of intermolecular anchoring as a strategy to develop high-performance piezoelectric composites for wearable electronics.

Piezoelectric materials are critical to develop advanced sensors and actuators<sup>1–7</sup>. Due to the intriguing attributes of light weight, flexibility, biocompatibility and easy processibility, polyvinylidene fluoride (PVDF) and its copolymers have been widely employed in the fields of sensing, transducing and energy applications<sup>8–13</sup>. The piezoelectricity of PVDF composites is mainly determined by the crystalline phases and

spontaneous polarization, where the  $\alpha$  phase has TGTG' (T-*trans*, G-*gauche*<sup>+</sup>, G'-*gauche*<sup>-</sup>) dihedral conformation with a dihedral angle of  $\pm 60^\circ$ , while the  $\beta$  phase has all-*trans* (TTTT) conformation with a dihedral angle of  $180^\circ$  and the  $\gamma$  phase has kinked conformation of TTTGTTG'. Among these, the  $\beta$  phase is the most electroactive polar phase, exhibiting excellent piezoelectric, pyroelectric and ferroelectric

<sup>1</sup>State Key Laboratory of Electronic Thin Films and Integrated Devices, School of Optoelectronic Science and Engineering, University of Electronic Science and Technology of China, 610054 Chengdu, China. <sup>2</sup>Department of Materials Science and Engineering, The Pennsylvania State University, State College, PA 16802, USA. <sup>3</sup>Department of Bioengineering, University of California, Los Angeles, Los Angeles, CA 90095, USA. <sup>4</sup>Electronic Materials Research Lab, Key Lab of Education Ministry/International Center for Dielectric Research, School of Electronic and Information Engineering, State Key Laboratory for Mechanical Behavior of Materials, Xi'an Jiaotong University, 710049 Xi'an, China. <sup>5</sup>School of Materials Science and Engineering, Research Center for Materials Genome Engineering, Wuhan University of Technology, 430070 Wuhan, China. <sup>6</sup>These authors contributed equally: Yuanjie Su, Weixiong Li, Xiaoxing Cheng, Yihao Zhou. ✉ e-mail: [tuy123@psu.edu](mailto:tuy123@psu.edu); [libei@whut.edu.cn](mailto:libei@whut.edu.cn); [ful5@xjtu.edu.cn](mailto:ful5@xjtu.edu.cn); [jun.chen@ucla.edu](mailto:jun.chen@ucla.edu)

properties<sup>14</sup>. Accordingly, obtaining the  $\beta$  phase is essential for improving the piezoelectricity of fluoropolymers. To this end, various processing methods were utilized to induce dipole alignment for increasing the electroactive  $\beta$  phase content including mechanical stretching<sup>15</sup>, electric poling<sup>16</sup> and thermal annealing<sup>17</sup>. Meanwhile, the inclusion of TrFE monomers into PVDF chains can also modify the crystallization kinetics of PVDF films and lead to morphotropic phase boundary (MPB)-like behaviors (e.g., the high piezoelectric activity) in piezoelectric polymers<sup>8,11,18–20</sup>. By synergizing the merits of both high-performance piezoelectric ceramics and flexible fluoropolymers, the piezoelectric composites are the choice of materials for next-generation on-body bioelectronics toward widespread scenarios, such as soft robotics<sup>21</sup>, biomonitoring<sup>22–26</sup>, and human-machine interface<sup>5,13,27</sup>. Nevertheless, the random distribution and complex connectivity of ceramic fillers within the fluoropolymer matrix cause inhomogeneity and discontinuity of inorganic-organic interfaces, which hampers the long-range alignment of dipole moments in the polymeric chains and thus the all-*trans* conformation (i.e., polar  $\beta$ -phase)<sup>28–30</sup>. Meanwhile, the large discrepancy in dielectric permittivity between ceramic fillers and polymer matrix dramatically weakens the applied electric field in the ceramics during electric poling and thereby restricts the domain evolution and permanent polarization<sup>31–33</sup>. Consequently, it is highly desired to develop high-performance piezoelectric composites with long-range all-*trans* conformation and strong polarization.

In order to promote and stabilize the ratio of the polar  $\beta$ -phase, versatile fillers such as carbon nanotubes<sup>34</sup>, silver nanowires (AgNWs)<sup>6,35</sup>, ferrites<sup>36–39</sup>, graphene oxide (GO) and reduced graphene oxide (rGO) salts<sup>40–42</sup> have been introduced as a nucleating agent to maximize and maintain the zigzag alignment of methylene ( $-\text{CH}_2$ ) and difluoromethylene ( $-\text{CF}_2$ ) groups within the polymer chains. Note that functional groups of the GOs and their derivatives are conducive to forming dipole moment reinforcements to sustain the residual orientation of  $\beta$ -phase nanocrystals<sup>40</sup>. Meanwhile, the essential factor for the nucleation of the  $\beta$ -phase in the PVDF nanocomposites lies in the static electric interaction between the fillers with a negative zeta potential and the  $-\text{CH}_2$  groups having a positive charge density<sup>35–38</sup>. Despite the formation of  $\beta$ -phase could be facilitated partially by doping nanofillers, the sparse functional groups, discontinuous interface, low compatibility and inability to align domain on a large-scale of conductive fillers make it rather challenging to attain a homogeneous and long-range molecular interaction with PVDF molecular chains<sup>43,44</sup>, which significantly hinders the dipole polarization and thus the all-*trans* conformation of the as-synthesized polymer composites. Meanwhile, the mechanism of domain alignment enabled by intermolecular interaction at the inorganic-organic interfaces in piezoelectric composites is still unclear and underexplored.

Herein, we demonstrate a simple and efficient strategy for tailoring the local dipole moment and  $\beta$  phase content of piezoelectric polymer composites by introducing  $\text{Ti}_3\text{C}_2\text{T}_x$  MXene nanosheets. Employing phase-field simulation and molecular dynamics (MD) calculations, we show that OH surface terminations on the  $\text{Ti}_3\text{C}_2\text{T}_x$  nanosheets offer hydrogen bonding with the fluoropolymer matrix, leading to dipole alignment and enhanced net spontaneous polarization of the polymer-ceramic composites. We then translated this interfacial bonding method into electrospinning to rationalize the piezoelectric properties of samarium doped PMN-PT/PVDF (Sm-PMN-PT/PVDF) nanofibers via  $\text{Ti}_3\text{C}_2\text{T}_x$  nanosheets inclusion. It was found that an appropriate loading (2.5 wt%) of  $\text{Ti}_3\text{C}_2\text{T}_x$  flakes below the percolation threshold effectively strengthen the polarization efficiency and interfacial coupling between the inorganic nanofillers and the organic polymer matrix, promoting the piezoelectricity by 160 % in comparison with the undoped version. Toward practical application, a soft piezoelectric textile (PT) sensor was developed by electrospinning the MXene-enabled piezoelectric composite (MPC), which can be

integrated into shoe insole for continuous gait patterns monitoring, walking habits identification, and Metatarsalgia prognosis.

## Results

### MD simulation of $\text{Ti}_3\text{C}_2\text{T}_x$ enabled intermolecular anchoring effect

$\text{Ti}_3\text{C}_2\text{T}_x$  nanosheets were exfoliated from the  $\text{Ti}_3\text{AlC}_2$  MAX phase by selectively etching Al layers using a HCl/LiF solution, during which the surface transition metal spontaneously reacts with water or fluoride ions to produce hydroxyl ( $-\text{OH}$ ), oxygen ( $-\text{O}$ ), and fluoro ( $-\text{F}$ ) surface terminations. These abundant functional groups terminated on the  $\text{Ti}_3\text{C}_2\text{T}_x$  lamellae arising from chemical etching are favorable for designing hydrogen, ionic and covalent linkage with surrounding dielectrics<sup>45–47</sup>. To this end,  $\text{Ti}_3\text{C}_2\text{T}_x$  nanosheets were employed to establish hydrogen bonds and electron-dipole interaction with C–H and C–F moieties of the PVDF molecules, enabling strong intermolecular bindings with PVDF polymer chains as shown in Fig. 1a. The local anchoring of PVDF chains on the two-dimensional MXene platelets directs in-situ alignment and orientation of  $\text{CH}_2$  and  $\text{CF}_2$  moieties and therefore transition from initial randomly coiled conformations (left part of Fig. 1a) to long-range all-*trans* conformation (right part of Fig. 1a), enlarging the macroscopic out-of-plane polarization and piezoelectricity.

To understand the interaction between the  $\text{Ti}_3\text{C}_2\text{T}_x$  nanosheets and fluoropolymer, MD calculations were implemented using the periodic lattice of  $\text{Ti}_3\text{C}_2\text{T}_x$  with  $-\text{OH}$  surface terminations and 60 “mer” chains of PVDF (Fig. 1b). To better illustrate the functionality and mechanism of hydrogen bonds between  $-\text{OH}$  group and  $-\text{CF}_2$  moieties of the PVDF, the corresponding MXene flakes functionalized with  $-\text{O}$  termination (Fig. 1c) were also constructed and calculated with the same number of “mer” chains. Apparently, after 2000 ps interaction, the PVDF chains anchored on the  $\text{Ti}_3\text{C}_2(\text{OH})_2$  lamellae accomplish an out-of-plane polarization of 371.42 D under electrical poling while the counterpart versions on the  $\text{Ti}_3\text{C}_2\text{O}_2$  platelets trigger an out-of-plane polarization of 308.13 D (Supplementary Fig. 1), suggesting the enhancement of self-assembly of highly aligned PVDF chains on the  $\text{Ti}_3\text{C}_2(\text{OH})_2$  flakes via the intermolecular interaction enabled by hydrogen bonding. Additionally, the pulling force needed to apply on each atom of the single PVDF chain is respectively 2.919 pN and 1.807 pN for  $\text{Ti}_3\text{C}_2(\text{OH})_2$  and  $\text{Ti}_3\text{C}_2\text{O}_2$  to initialize the separation (Fig. 1d), implying a stronger interaction and tighter locking between  $\text{Ti}_3\text{C}_2(\text{OH})_2$  flakes and PVDF chains. Without hydroxyl groups to guide the alignment of moieties of the PVDF molecule, the dipoles within the PVDF matrix would present irregular distribution to minimize the internal electrostatic energy (Supplementary Figs. 2, 3).

The phase transition could be clearly reflected from the variation of dihedral angles in bond conformation within the PVDF chains, where the most favorable torsional bond arrangement has substituents at  $180^\circ$  (*trans* or T) to each other instead of the ones at  $\pm 60^\circ$  (*gauche* or G)<sup>14</sup>. Notably, the  $-\text{OH}$  functionalized  $\text{Ti}_3\text{C}_2\text{T}_x$  platelets possess a higher proportion of bond conformation near  $180^\circ$  (Fig. 1f) but a lower fraction of bond conformation near  $-60^\circ$  (Fig. 1e and Supplementary Fig. 4) vice versa, indicating the transform from the *gauche* conformation to *trans* conformation as a consequence of hydrogen bonding induced anchoring effect. Interestingly, according to the MD calculation,  $\text{Ti}_3\text{C}_2(\text{OH})_2$  platelets give rise to a higher fraction of T bond fraction (Supplementary Fig. 5) and TTTT (all-*trans*) conformation (Fig. 1g) in the PVDF chains in comparison with that of  $\text{Ti}_3\text{C}_2\text{O}_2$ , which validates the role and functionality of hydrogen bonds in terms of arrangement and orientation of polymer chains toward all-*trans* conformation (i.e., polar  $\beta$  phase), promoting the net spontaneous polarization and the piezoelectricity of the fluoropolymer composites. Aside from the PVDF, the  $\beta$ -phase content and polarization of poly(vinylidene fluoride-co-trifluoroethylene) (P(VDF-TrFE)) copolymers can also be enhanced by this proposed MXene anchoring method

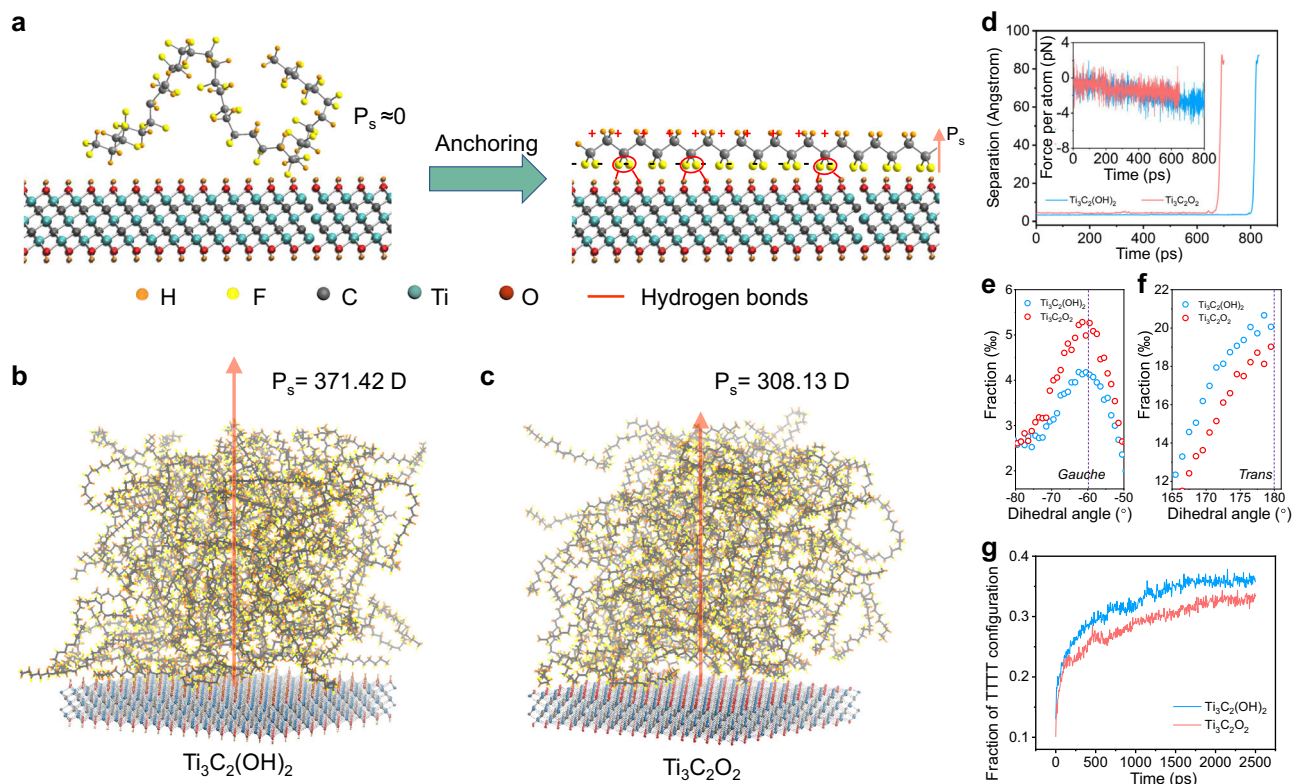


**Fig. 1 | Hydrogen bonds induced anchoring effect enabled by MXene nanosheets.** **a** Schematic of in-situ stretching and alignment of PVDF polymer chain via surface terminations on  $\text{Ti}_3\text{C}_2\text{T}_x$  nanosheets to upgrade the spontaneous polarization ( $P_s$ ). **b, c** Final snapshots for molecular dynamics (MD) simulations of the polarization of PVDF polymer film on the  $\text{Ti}_3\text{C}_2(\text{OH})_2$  flakes (**b**) and  $\text{Ti}_3\text{C}_2\text{O}_2$  flakes

(**c**). **d** Simulated separation of a single PVDF chain away from  $\text{Ti}_3\text{C}_2(\text{OH})_2$  and  $\text{Ti}_3\text{C}_2\text{O}_2$  flakes upon pulling. Inset: The pulling force applied on each atom needed to separate the PVDF chain from MXene flakes. **e, f** Dihedral angles distribution of PVDF chains near the  $-60^\circ$  (*Gauche*, **e**) and  $180^\circ$  (*Trans*, **f**) averaged over the last 500 ps. **g** Fraction of TTTT configuration as a function of time.

according to the MD simulation (Supplementary Figs. 6, 7), validating the universality and feasibility.

### Design of MXene/Sm-PMN-PT/PVDF nonwoven piezoelectric composites

To bring the aforementioned proposed principle and strategy into reality, electrospinning was adopted to construct MXene doped fluoropolymer due to its inherent merit of integrating in-situ stretching with local poling in one step. Figure 2a elucidates the synthesis procedure and composition of the MXene/Sm-PMN-PT/PVDF nonwoven piezoelectric composites, in which a suspension of MXene powder, Sm-PMN-PT particles and PVDF was used as a precursor for subsequent electrospinning (Supplementary Fig. 8). Sm-PMN-PT was selected as the ceramic fillers because of its large piezoelectric coefficient ( $-1500 \text{ pC/N}^2$ ) in comparison with the conventional piezoelectric ceramics such as BTO ( $-190 \text{ pC/N}^{48}$ ), PZT ( $560 \text{ pC/N}^{49}$ ) and PMN-PT ( $-620 \text{ pC/N}^3$ ) (bottom inset of Fig. 2a). Meanwhile, in addition to intermolecular linkage bound with PVDF polymer chain (upper inset of Fig. 2a), the introduction of MXene lamellae efficiently enhances the conductivity and mechanical ductility of the precursor and thus promotes the subsequent local electric poling and in-situ mechanical stretching of polymer composites during electrospinning, which is beneficial to achieving the zigzag alignment of  $-\text{CH}_2$  and  $-\text{CF}_2$  and thus the all-*trans* conformation within PVDF polymer (Supplementary Fig. 9).

Figure 2b reveals the morphology and element structure of the as-synthesized piezoelectric nonwoven textiles consisting of randomly stacked molten PVDF/Sm-PMN-PT/MXene nanofibers through the electrospinning method. The incorporation of MXene nanosheets exhibits a negligible impact on the morphology of the fibrous configuration (Supplementary Fig. 10). Energy-dispersive spectrometer

(EDS) mapping spectra of Pb, F, and Ti elements further confirms the uniform distribution of Sm-PMN-PT, PVDF and MXene in the composite films (Fig. 2b and Supplementary Fig. 11). Note that the formation of  $\text{TiO}_2$  originates from the oxidation of MXene on the surface (Supplementary Figs. 12, 13). According to the high-resolution transmission electron microscope images, PVDF polymeric chains aligning along the inorganic-organic interface validate the zigzag alignment of  $-\text{CH}_2$  and  $-\text{CF}_2$  (Fig. 2c). In addition, X-ray photoelectron spectrometer (XPS) spectra (Fig. 2d and Supplementary Fig. 14) evidently demonstrates that the oxygen functionalities and hydrogen bonds were anchored on the surface of the as-synthesized nanofibers, where the emerging peaks of C–O and C=O groups resulting from the MXene incorporation suggest that strong interactions such as hydrogen bonds are formed between the  $-\text{OH}$  and  $-\text{O}_x$  functional groups in the MXene flakes and the  $-\text{CF}_2$  groups within PVDF, evidencing the aforementioned hypothesis. Higher binding energy peaks observed in O 1s region (Supplementary Fig. 15) for C–Ti–O and C–Ti–OH demonstrate that hydroxy termination is dominant on the surface of the flakes.

Figure 2e elucidates the X-ray diffraction (XRD) pattern of the as-synthesized nanofibers and pristine MXene and Sm-PMN-PT powders. The characteristic  $2\theta$  peak of the  $\text{Ti}_3\text{C}_2\text{T}_x$  lamellae is  $6.48^\circ$  corresponding to (002) lattice plane with a d-spacing of  $13.66 \text{ \AA}$ , indicative of successful removal of the Al atom layer from the multilayer  $\text{Ti}_3\text{AlC}_2$  MAX phase during the chemical etching process (Supplementary Fig. 16)<sup>50</sup>. Apparently, the peak intensity (002) of the composites is lower than that of the pristine MXene as the addition of PVDF molecules enhances the distance between MXene flakes. Furthermore, six diffraction peaks at  $20.5^\circ$ ,  $31.4^\circ$ ,  $38.5^\circ$ ,  $44.7^\circ$ ,  $50.4^\circ$  and  $56.1^\circ$  were ascribed to the crystal planes of (100), (110), (111), (200), (210), and (211), respectively. The existence of these peaks confirms that the Sm-PMN-PT ceramic fillers in the composite film retain polycrystalline

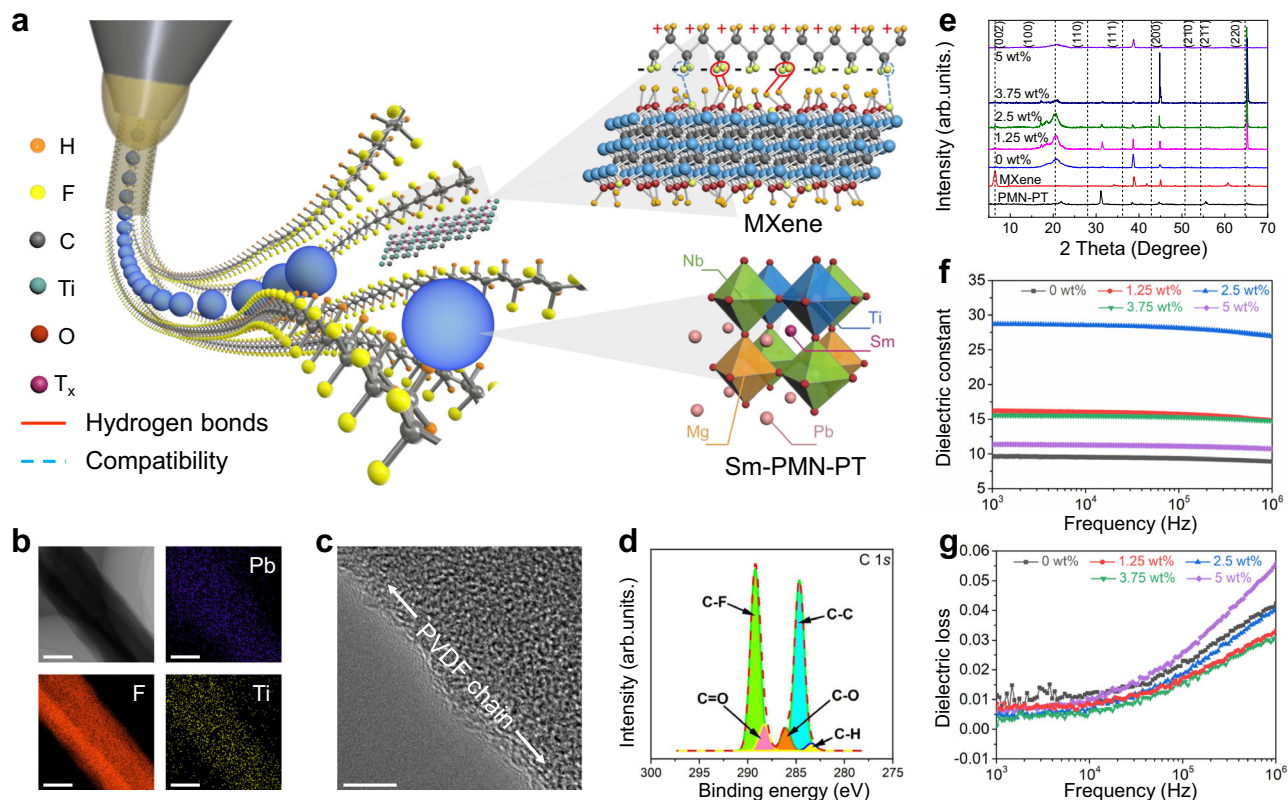


**Fig. 2 | Structure design and characterization of the MXene-enabled piezoelectric composite (MPC) based soft piezoelectric textile (PT).** **a** Schematic illustration of electrospinning procedure for MPC textiles synthesis. Inset: Inter-molecular interaction between MXene and PVDF; and  $2 \times 2 \times 2$  supercell of Sm-PMN-PT as a ceramic filler. **b** Scanning electron microscope (SEM) images and Energy-dispersive spectrometer (EDS) mapping spectra of Pb, F, and Ti elements in the as-prepared composite film. Scale bars: 200 nm. **c** High resolution SEM image of

an as-electrospun single fiber. Scale bar: 5 nm. **d** C 1s X-ray photoelectron spectrometer (XPS) spectra of as-prepared PT. **e** X-ray diffraction (XRD) spectra of undoped textiles and the prepared MPC textile with varying MXene mass fractions. **f** Frequency-dependent dielectric permittivity of fabricated MPC textile with diverse MXene mass fractions. **g** Frequency-dependent dielectric loss of fabricated MPC textile with diverse MXene mass fractions.

perovskite structure<sup>51</sup>. In addition, the typical diffraction peak at  $20.5^\circ$  for the crystal plane of (110) maximizes at the  $\text{Ti}_3\text{C}_2\text{T}_x$  mass fraction of 2.5 wt%, indicating a larger ratio of local all-*trans* conformation (polar  $\beta$  phase) when compared with other versions.

The frequency dependencies of dielectric relative permittivity and dielectric loss of as-prepared MPC textiles and undoped textiles were respectively presented in Fig. 2f, g as a function of MXene inclusion amount at room temperature. The dielectric permittivity for all the samples slightly declines with increasing frequency as a consequence of relaxation (Fig. 2f). It is found that the dielectric permittivity pronouncedly undulates with MXene doping amount and reaches a maximum at 2.5 wt% over a frequency range of 1 kHz–1 MHz, while the dielectric loss maximizes at 5 wt%. This is because the proper inclusion of conductive MXene nanosheets is favorable for interfacial polarization between fillers and polymer matrix, whereas the excessive addition of MXene into polymer composites gives rise to an augmented leaking current and thereby a larger dielectric loss.

### Characterization and phase-field simulation

To further analyze the interfacial coupling effect between the fluoropolymer matrix and the inclusion, piezoelectric force microscopy (PFM) is employed to assess the ferroelectric and piezoelectric properties of as-electrospun nanofibers with or without MXene doping. The PFM amplitude, PFM phase, phase-field simulated domain structure, and MD calculated polarization were presented for a single undoped Sm-PMN-PT/PVDF fiber (Fig. 3a–d) and a MPC fiber (Fig. 3e–h). The PFM results show a larger area of single ferroelectric domain observed in the MPC fiber in comparison with that in the undoped fiber,

implying an enhanced piezoelectric response after MXene addition. This was both certified by the phase-field simulation (Fig. 3c, g) of the ferroelectric domain structure and MD calculation results (Fig. 3d, h) that the out-of-plane domain size of polymer composite becomes larger in the vicinity of the ceramic particle by adding MXene flakes. The phase-field simulation reveals a multi-domain state with 180 degrees domains in the polymer matrix for both undoped and MPC fibers, where the MPC fiber possesses a larger domain fraction with polarization aligned along the poling direction (PD) of electrospinning compared with that of the undoped fiber. Moreover, the embedded Sm-PMN-PT particle maintains a polycrystalline structure as its coercive field is much higher than the in-situ poling field (1.2 kV/cm) of electrospinning<sup>2</sup>.

The modulated dipole structure of MPC fibers with increased polarization further gives rise to an increased piezoelectric response. PFM measurements show that all the as-synthesized electrospun fibers exhibit a butterfly-shape hysteresis of the amplitude versus bias, where the MPC fiber displays a higher amplitude (Fig. 3j) than the undoped one (Fig. 3i), implying a larger piezoelectric coefficient ( $d_{33}$ ). As displayed in Fig. 3k, the  $d_{33}$  derived from PFM test first increases and then decreases upon increasing the MXene doping amount, with a maximum  $d_{33}$  achieved at 2.5 wt% of MXene. It is worth noting that both phase-field simulation and MD calculation follow a similar changing tendency of polarization as well as out-of-plane domain proportion to the PFM results (Fig. 3l), which verifies the accuracy and reliability of our proposed theoretical modeling.

To achieve a more intuitive understanding of the functionality and mechanism of MXene lamellae addition, a schematic was utilized

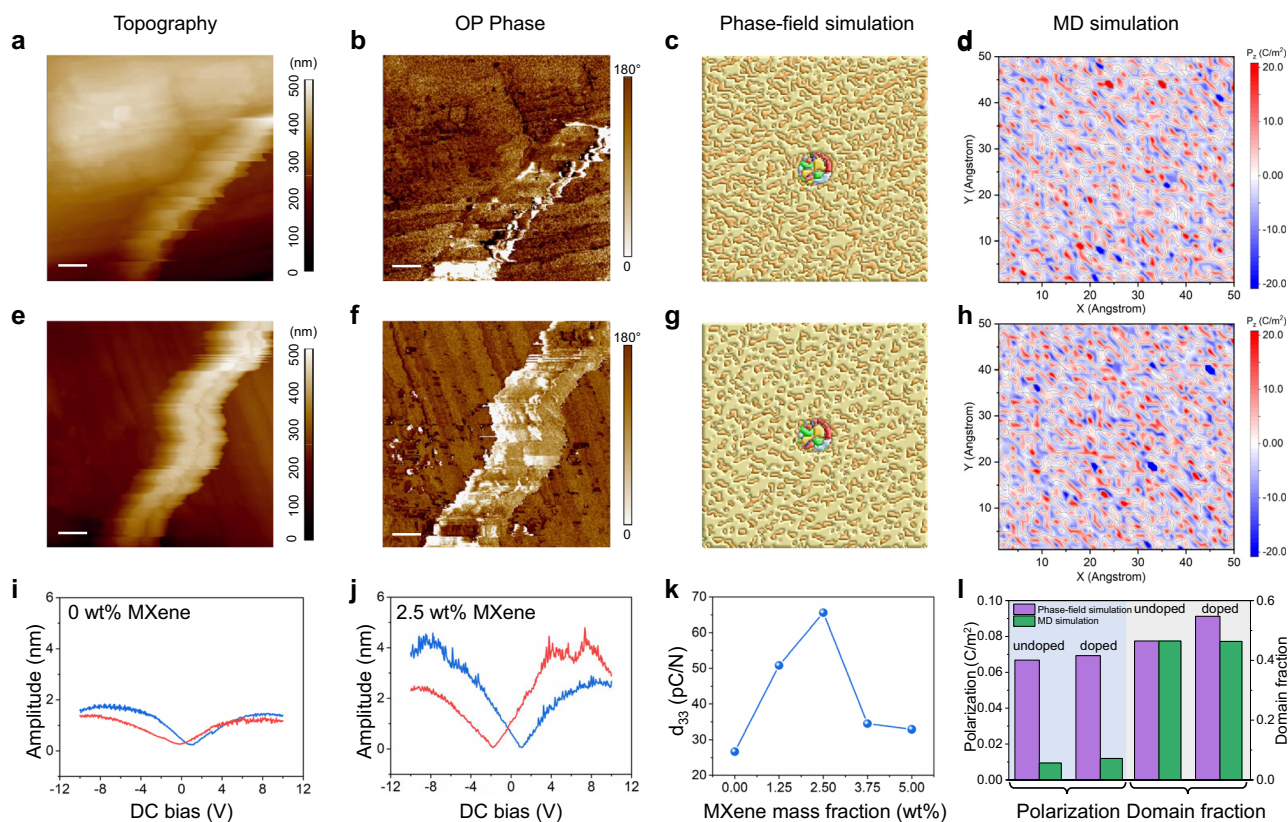


**Fig. 3 | Characterization and simulations for the as-synthesized electrospun fibers.** **a–d** Piezoelectric force microscope (PFM) Topography (**a**), Out-of-plane (OP) PFM phase image (**b**), phase-field simulation of domain structure (**c**), MD calculation of polarization (**d**) of a single undoped nanofiber. Scale bars: 200 nm. **e–h** PFM Topography (**e**), PFM phase image (**f**), phase-field simulation of domain structure (**g**), MD calculation of polarization (**h**) of a single MPC nanofiber. Scale

bars: 200 nm. **i, j** PFM characterized butterfly amplitude loops for undoped fibers (**i**) and 2.5 wt% MXene doped fibers (**j**) under a direct current (DC) bias from  $-12$  V to  $12$  V. **k** The PFM measured piezoelectric coefficient ( $d_{33}$ ) of as-prepared nanofibers as a function of MXene mass fractions. **l** Comparison of the phase-field simulation and MD simulation of the spontaneous polarization and out-of-plane domain fractions for the undoped and MXene-doped samples.

to elaborate the  $\beta$  crystalline phase conformation and orientation during the electrospinning of the MXene/Sm-PMN-PT/PVDF composites. For bare PVDF nanofibers (Fig. 4a),  $\beta$  phase crystalline can be partially aligned by the in-situ poling while some localized amorphous microstructures still exist. The situation was changed once a small amount of MXene (1.25 wt% and 2.5 wt% in our case) is added into the PVDF-based composite, as shown in Fig. 4b. In addition to the hydrogen bonds formed between PVDF chains and MXene sheets, the applied electric field yields inductive charges on the surface of conductive MXene nanosheets and thereby provokes a greater Coulomb force during the electrospinning. This electrostatic force further attracts PVDF chains to crystallize on the MXenes surface in the zigzag arrangement, which expedites the transformation of local amorphous regions into the  $\beta$  crystalline phase. Consequently, the  $\beta$  phase is enhanced when compared with pure PVDF nanofibers (Fig. 4a). However, superfluous addition leads to a stack of MXene nanosheets and suppresses the orientation and alignment of polymeric chains in the way of forming  $\beta$  phase crystalline. In the meantime, the connection of these stacked MXene flakes boosts the leaking current, which hinders the effective dielectric permittivity ( $\epsilon_{33}$ ) and piezoelectric coefficient ( $d_{33}$ ) of the composite. To verify this proposed modeling on the crystallinity and phase shift, the Fourier transform infrared (FTIR) spectrum of the undoped textiles and MPC textiles doped with various MXene mass fractions were revealed in Fig. 4d. The adsorption peaks at  $763\text{ cm}^{-1}$  and  $973\text{ cm}^{-1}$  are attributed to  $\alpha$ -phase crystalline structure of PVDF and the adsorption peak at  $841\text{ cm}^{-1}$ ,  $1276\text{ cm}^{-1}$  and  $1429\text{ cm}^{-1}$  are ascribed to a  $\beta$ -phase crystalline structure<sup>52</sup>. According to Beer-Lambert equation<sup>5</sup>, the fraction of the  $\beta$  phase ( $F_{\beta}$ ) of as-synthesized nanofibers can be

attained as a function of MXene loading amount (Supplementary Fig. 17), where the highest  $\beta$  phase of 83.4% occurs at the loading of 2.5 wt% MXene. Consequently, the phase evolution trend upon MXene doping revealed by the FTIR test agrees well with the proposed principle.

To further testify the above hypothesis and shine some light on the mechanism, phase-field simulation was carried out to numerically illustrate the impact of conductive fillers on the domain structure and polarization of the ferroelectric composites. As shown in Fig. 4e–g, incorporation of a proper content (2.5 wt%) of MXene lamellae notably improves the polarization of the as-electrospun composite, whereas further accretion jeopardizes the polarization and may even cause it to fall below the undoped counterpart (Fig. 4h), which is in good accordance with foregoing deduction and FTIR test. Furthermore, as for the simulated domain structure (Fig. 4i–k), the incorporation of MXene drives the polarization toward the out-of-plane direction parallel to the electrospinning poling field when compared with the undoped one, which is also consistent with the PFM results. A loading of 2.5 wt% MXene contributes to an enhancement of the volume fraction of PD out-of-plane domain from 67.8 to 72.6% (Fig. 4l and Supplementary Figs. 18, 19). It is believed that the net out-of-plane domain is responsible for the augmented  $\beta$  phase content and corresponding larger piezoelectric response. Given that the piezoelectric coefficient is proportional to spontaneous polarization and permittivity ( $d_{33} = 2P_s\epsilon_{33}Q_{33}$ ), a proper doping of the conductive component is proven to be an efficient approach to upgrade the piezoelectric performance of polymer composites.

To understand the role of MXene doping on the percolation effect in the as-electrospun composites nanofibers, a phase-field simulation

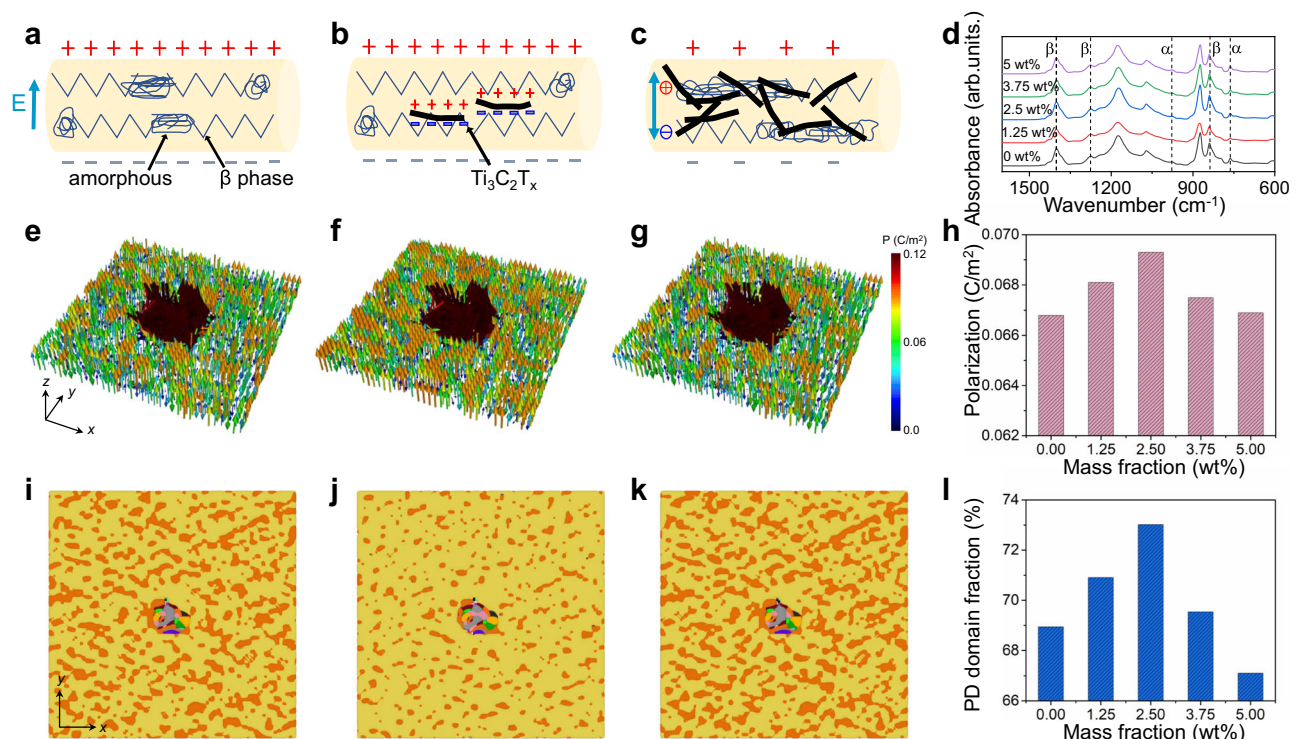


**Fig. 4 | Mechanism of as-electrospun nanofibers via doping MXene nanosheets.** **a–c** Schematic of the polarization process of electrospun nanofibers doped with **a** no MXene, **(b)** proper amount of MXene, and **(c)** excessive amount of MXene. **d** Fourier transform infrared (FTIR) spectrum of the undoped textiles and the prepared MPC textiles with varying MXene mass fractions. **e–g** Simulated polarization field in the vicinity of Sm-PMN-PT particle in the nanocomposites doped

with **e** no MXene, **(f)** proper amount of MXene, and **(g)** excessive amount of MXene. **h** Calculated polarization of the MPC textiles doped with various MXene amount. **i–k** Simulated domain structure in the vicinity of Sm-PMN-PT particle in the nanocomposites doped with **i** no MXene, **(j)** proper amount of MXene, and **(k)** excessive amount of MXene. **l** Calculated poling direction (PD) domain fraction of the prepared textiles as a function of MXene doping amount.

of effective properties was implemented to analyze the dependence of the MXene doping amount on the dielectric, piezoelectric and mechanical properties of the electrospun unmodified and MPC textiles. As displayed in Fig. 5a, a three-dimensional fibrous configuration was randomly computer-generated to imitate the structure of electrospun nonwoven textiles (Supplementary Fig. 10). The stress distribution, electric field and electric potential of MPC textiles under constant applied stress of  $1 \times 10^6$  Pa along the out-of-plane (z) direction are calculated. As displayed in Fig. 5b, the calculated piezoelectric coefficient  $d_{33}$  and dielectric permittivity  $\epsilon_{33}$  undulate with increasing MXene mass fraction from 0 to 5.0 wt%, reaching a maximum value at 2.5 wt%. A similar trend is observed on both the  $d_{33}$  meter measured  $d_{33}$  value and the calculated strain-induced piezoelectric polarization, two of which fluctuate with the loading of MXene flakes and reaches a maximum at 2.5 wt% (Fig. 5c and Supplementary Fig. 20). On the other hand, the stiffness coefficient retains almost the same at low MXene doping amount but remarkably decreases at high MXene doping level, indicating a hardening of the composites with high contents of doped MXene flakes.

### MPC textiles for energy harvesting and sensing

To explore the device performance of the fabricated MPC textiles in response to external stimulation, the output piezoelectric signals were systematically characterized under a diversity of applied forces varying from 1 to 9 N, as plotted in Fig. 5d, e. Notably, the electric outputs of the MPC textiles are proportional to applied stress and the MXene doped devices deliver larger voltage and current than the unmodified version. Furthermore, under a fixed external force of 3 N, the signal intensity varies with the changing doping amount of MXene and the 2.5 wt% MXene doped nanocomposite yields a gain of 160% when compared with the undoped sample (Supplementary Figs. 21,

22). It is worth pointing out that the electric outputs follow an analogous changing tendency as the calculated piezoelectric coefficient upon conductive filler doping (Fig. 5e), which convincingly confirmed the validation and feasibility of our proposed theoretical modeling and corresponding calculation. Consequently, all the following measurements were carried out using an optimal MXene mass fraction of 2.5 vol% because of its favorable piezoelectric properties. Figure 5f shows the impedance response of the prepared MPC textile doped with 2.5 wt% MXene under various resistances from 10 KΩ to 100 GΩ, where the maximum output power was achieved at 80 MΩ. The mechanical stretchability and robustness of as-synthesized MPC textiles were testified by the long-term fatigue test as illustrated in Fig. 5g, where the output voltage retains a constant value when subjected to more than 7000 cycles of 5 N impact force application, demonstrating an excellent mechanical robustness and reliability for practical scenarios.

To verify the sensing capability of MPC textile for active biomonitoring, a self-powered gait monitoring system was developed. As schemed in Fig. 6a, by attaching as-synthesized devices onto five different positions (M1–M5) of a conventional insole (see Supplementary Note 1, Supplementary Figs. 23, 24 for details), the stress distribution of the foot can be spontaneously detected. It can be clearly seen that the incorporation of MXene triggers a much larger amplitude of output charge than the undoped one when the big toe pressing the device on site of M5 (Fig. 6b) regardless of walking postures including pigeon-toed, normal and splayfooted (Fig. 6c). Furthermore, various gait patterns of walking, running, jumping, falling forward, and falling backward can be accurately recognized and distinguished with regards to the dynamic signal mapping among the five units (Fig. 6d and Supplementary Movie 1). It is interesting that the falling forward and falling backward possess adverse signal mapping profiles due to the

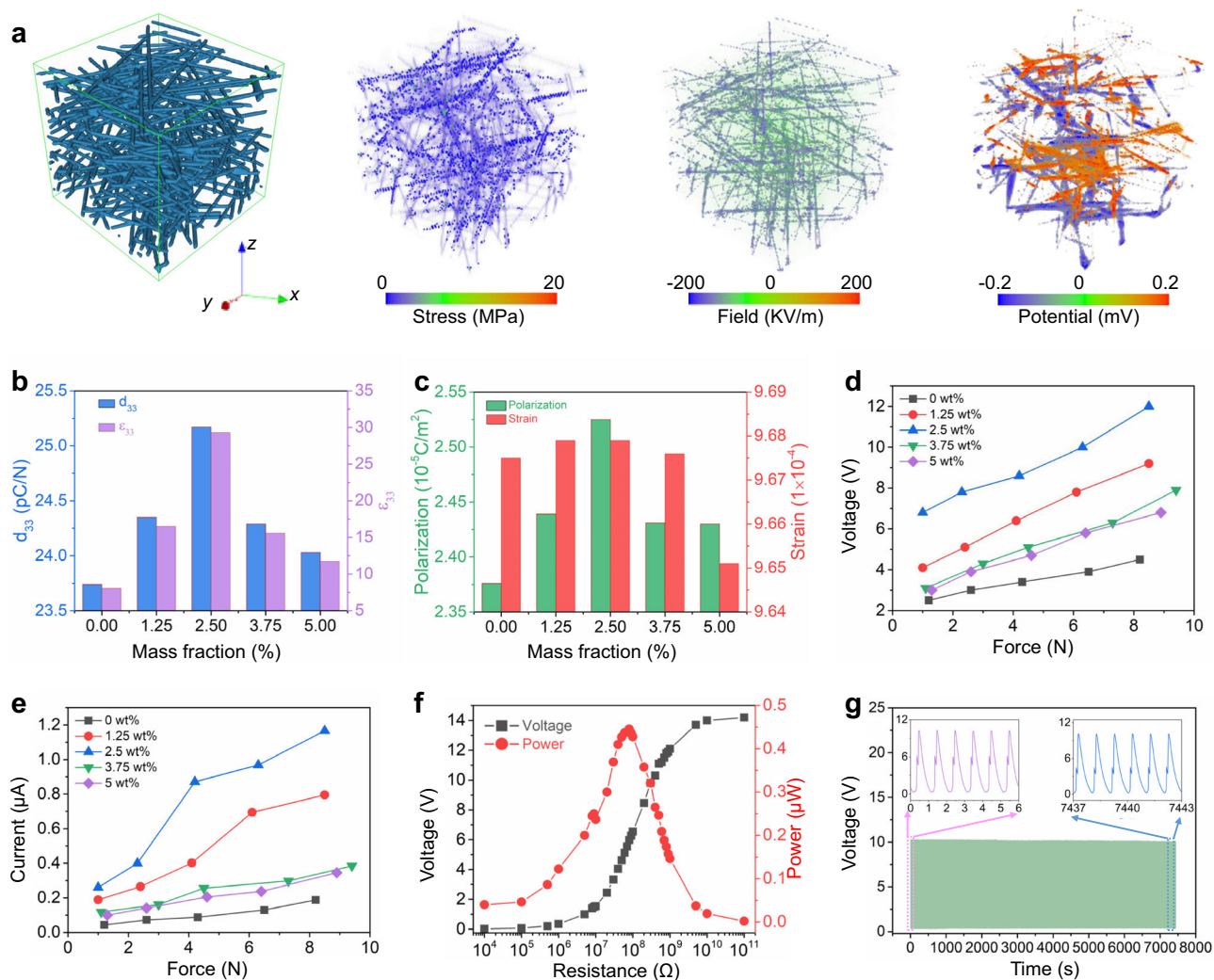


**Fig. 5 | Characterization and phase-field simulation results of the as-electrospun textiles.** **a** The visualized structural modeling, stress distribution, electric field distribution, and piezoelectric potential distribution of as-prepared MPC textiles. Note: The applied stress is fixed at  $10^6$  Pa along the z-axis for the simulation. **b** The calculated piezoelectric coefficient ( $d_{33}$ ) and dielectric constant ( $\epsilon_{33}$ ) of the as-electrospun textiles doped with various MXene mass fractions. **c** The

calculated average polarization and strain of the as-electrospun textiles doped with various MXene mass fractions. **d, e** Output voltage (**d**) and current (**e**) of the as-electrospun textiles as a function of applied mechanical force. **f** Impedance response of prepared 2.5 wt% MXene doped MPC. **g** Durability of the as-prepared MPC.

opposite moving direction of the falling body. Meanwhile, the signal profile of walking, running, and jumping acquired by the five positions gradually rises up as a result of augmented stamped force exerted on the insole. Aside from the real-time pressure distribution recognition, the dynamic stride frequency and amplitude can be efficiently identified and recorded by the interval and amplitude of the signal waveforms, respectively (Supplementary Fig. 25). Note that even though the as-electrospun PTs might deliver smaller output signals than the triboelectric devices<sup>33</sup>, they do not need an extra mobile component like triboelectric devices to trigger electricity generation, allowing for all-in-one configuration and biocompatibility<sup>12</sup>. To demonstrate the potential of MPC textiles in identifying walking habits, the posture abnormality like pigeon-toed or splayfooted was further distinguished using the as-prepared smart insole (Fig. 6e and Supplementary Fig. 26). Apparently, the splayfoot renders a much higher pressure on the lateral side but lower pressure on the inner side of insole in comparison with the normal posture, which gives rise to a larger signal amplitude on position M1 and M3. In contrast, the pigeon-toed walking posture triggers a much higher pressure on the inner side but lower pressure on the lateral side of the insole when compared with the normal posture, leading to a larger amplitude on position M2, M4 and M5. Aside

from the gait monitoring, the prepared smart insole based on MPC textiles also reveals capability in clinic diagnosis. As a widespread foot condition, Metatarsalgia brings about a shape deformation of the metatarsal region and subsequent sharp pain in the ball of the foot. Figure 6f unveils and compares the walking signal profiles of a healthy person and a Metatarsalgia patient on the metatarsal region (M3, M4, M5). Due to the classical symptom of the curled toe, a signal contour with larger intensity on M5 and smaller intensity on M3 was recognized for the Metatarsalgia patient when compared to that of the healthy tester (Supplementary Fig. 27), which demonstrates the capacity of MPC textiles in clinic prognosis of Metatarsalgia.

## Discussion

A high-performance piezoelectric composite was fabricated via termination engineering using  $\text{Ti}_3\text{C}_2\text{T}_x$  MXene templating. To understand the interfacial coupling effect of the piezoelectric composites, PFM characterization in combination with phase-field simulation and MD calculation have been utilized to conduct a comprehensive analysis of the functionality and mechanism of MXene inclusion into ferroelectric polymer composites. A strong hydrogen bonding between the hydroxyl terminations on MXene nanosheets and  $-\text{CF}_2$

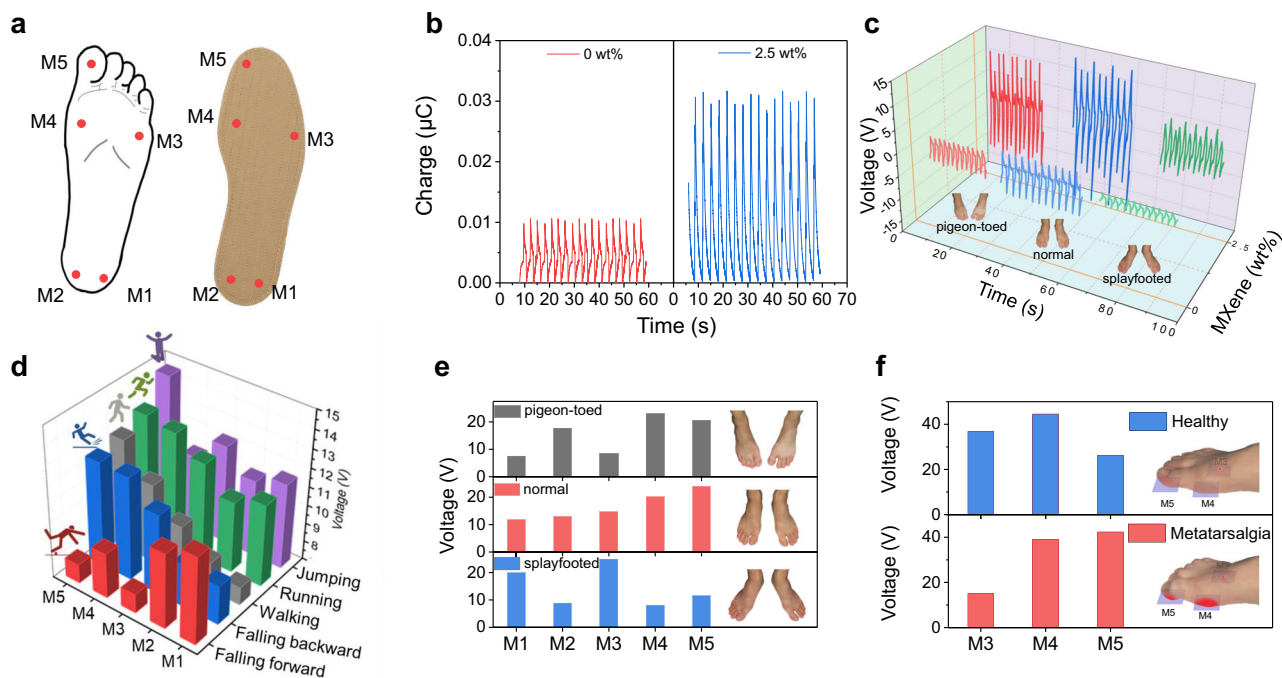


**Fig. 6 | Output performance and sensing application of as-prepared MPC based soft PT sensors.** **a** Schematic of a smart insole integrated with five PT sensors on five different sites to form a foot sensor network. **b** Piezoelectric charges of undoped fiber and MPC fiber on M5 site in response to an adult's (75 kg) toe

pressing. **c** Dynamic output voltages of undoped fiber and MPC fiber on M5 site when subjected to normal, pigeon-toed and splayfooted postures. **d–f** Signals profiles for gait monitoring (**d**), posture habits recognition (**e**), and Metatarsalgia prognosis (**f**).

moieties in PVDF chains is responsible for the long-range growth of TTTT configuration and alignment of domain orientation, which efficiently boosts the  $\beta$  phase content and piezoelectric coefficient. We then translated the hydrogen bond anchoring strategy into reality by synthesizing the  $\text{Ti}_3\text{C}_2\text{T}_x/\text{Sm-PMN-PT}/\text{PVDF}$  composites-based soft PTs via electrospinning. It is found that the incorporation of 2.5 wt%  $\text{Ti}_3\text{C}_2\text{T}_x$  into Sm-PMN-PT/PVDF composites leads to an output gain of 160% when compared with the undoped version. Furthermore, the as-electrospun MPC could be easily integrated into the conventional insole for active gait patterns monitoring, walking habits identification and Metatarsalgia prognosis. This work theoretically and experimentally looks into the underlying mechanism of the interfacial coupling effect of piezoelectric nanocomposites, opening up a paradigm for the development of high-performance wearable electronics.

## Methods

### Synthesis of Sm-PMN-PT piezoelectric ceramic particles

The composition of the Sm-PMN-PT is  $\text{Pb}_{0.97}\text{Sm}_{0.02}[(\text{Mg}_{1/3}\text{Nb}_{2/3})_{0.7}\text{Ti}_{0.3}]\text{O}_3$ .  $\text{MgNb}_2\text{O}_6$  powder was initially prepared using a solid-state reaction at 1200 °C.  $\text{Pb}_3\text{O}_4$ ,  $\text{MgNb}_2\text{O}_6$ ,  $\text{TiO}_2$ , and  $\text{Sm}_2\text{O}_3$  powders were mixed by ball-milling overnight as wet dispersion. Calcination of the mixed powders was conducted in a non-contaminated furnace at 850 °C for 2 h.

### Synthesis of layered MXene nanosheets

Firstly, 10 ml ultrapure water was utilized to dilute 30 ml 12 M hydrochloric acid solution (Chron chemicals Co., Ltd, China) to obtain 40 ml 9 M HCl. Subsequently, 2 g LiF (Aladdin, China) was added into 40 ml 9 M HCl followed by magnetic stirring for 5 min in order to obtain a hydrofluoric acid solution. Next, 1.2 g  $\text{Ti}_3\text{AlC}_2$  powder (MAX phase, purchased from 11 Technology Co., Ltd., China) was weighed and slowly added to the mixed solution for water bath stirring under a rotation speed of 400 rpm for 24 h at 35 °C. Then, the reaction product was centrifugated at  $1737 \times g$  for 5 min several times and rinsed with deionized (DI) water until the pH value reached 6. After suction

filtration and vacuum drying (45 °C, 24 h) followed by an ice bath ultrasonic, the MXene nanosheets were attained for spare.

### Fabrication of MPC textile-based sensor

First, the as-synthesized MXene powders of 0, 29.5, 59, 88.5, 118 mg, corresponding to the mass fraction of 0, 1.25, 2.5, 3.75, 5 wt% respectively, were dispersed in a beaker of 6 mL dimethylformamide (DMF) and 4 mL acetone mixed solvent and ultrasonically treated for 20 min to evenly disperse nanosheets in DMF solvent. Then, 118 mg Sm-PMN-PT nanoparticles together with 2.25 g PVDF powder were added into the mixed solution via magnetic stirring at 50 °C for 2.5 h in a water bath to obtain a stable and uniform electrospinning precursor solution. After solution agitation, ultrasonic treatment for 30 min allows nanoparticles to disperse evenly. Subsequently, the as-received solution was added into a 10 mL plastic syringe with a needle orifice of 25 gauge for electrospinning. The electrospinning was carried out for 2 h with a gap distance of 15 cm, a pushing speed of 0.6 mL/h and an electric field of 1.2 KV/cm at room temperature and 42% humidity (Zhiyan Technology Co., Sichuan). Then, as-electrospun textile was adhered by two pieces of aluminum tapes as electrodes and tailored into small pieces with a size of 3.0 cm  $\times$  3.0 cm. Finally, the whole device was packaged using PET substrates and transparent medical tape to build up a MPC textile-based sensor.

### Characterization and measurement

The  $d_{33}$  values were characterized using a ZJ quasi-static  $d_{33}$  meter developed by the Chinese Academy of Sciences with a frequency of 110 Hz and a mechanical load of 0.25 N. A Keithley 6514 electrometer system was used to collect the output signals of the prepared devices. The dielectric properties of the electrospun films were measured using an Agilent 4294A precision impedance analyzer with a film thickness of 15  $\mu\text{m}$  and an area of 1 cm  $\times$  1 cm. A field emission scanning electron microscopy (FESEM, Apero, Thermo, U.S.A.) was employed for morphology characterization. Piezoresponse force microscopy (PFM, NT-MDT Spectrum Instruments) was used to image the ferroelectric domain structures using a contact lithography mode with a tip



curvature radius of 35 nm and a tip height of 14–16  $\mu\text{m}$ , where an alternating-current voltage is applied to the metallic disk (=150 kHz,  $U_{\text{RMS}} = 0.5\text{V}$ ) and two Stanford Research 830R lock-in amplifiers are used to monitor the amplitude and phase of the deflection and torsion of the cantilever. Conductive Platinum-Iridium silicon cantilevers (NSG01/Pt) were used for the PFM characterization with detailed parameters listed in Supplementary Table 1. The phase purity and crystal properties of the samples were analyzed by an X-ray diffractometer (XRD: D8 Advance, Bruker-AXS, Germany) equipped with Cu-K $\alpha$  radiation ( $\lambda = 1.5418\text{ \AA}$ ). An XPS (ESCALAB 250Xi) was used with an Al K $\alpha$  excitation (1486.8 eV). The chemical composition and valence states were characterized by X-ray photoelectron spectroscopy (XPS, model ESCALAB 250, Al K $\alpha$ ,  $h\nu = 1486.6\text{ eV}$ ). The FTIR spectra were performed on Fourier infrared spectrometer (Smartlab 9, Rigaku, Japan). A linear motor with tunable frequency, amplitude, velocity and force was adopted to apply a diversity of stress and strain on the samples.

### Phase-field simulation of the ferroelectric domain structures

In the phase-field simulation, the time-dependent Ginzburg-Landau equation was employed to describe the evolution of the polarization<sup>34</sup> [Eq. 1],

$$\frac{\partial P_i(\mathbf{r}, t)}{\partial t} = -L \frac{\delta F}{\delta P_i(\mathbf{r}, t)}, \quad (i=1,2,3) \quad (1)$$

where  $L$  is the kinetic coefficient,  $t$  is the time,  $F$  is the total free energy of the system,  $\mathbf{r} = (x, y, z)$  is the spatial position vector, and  $P_i(\mathbf{r}, t)$  is the polarization field.  $\delta F / \delta P_i(\mathbf{r}, t)$  is the thermodynamic driving force for the spatial and temporal evolution of polarization.

The total free energy of the system includes contributions from the bulk free energy  $f_{\text{bulk}}$ , the elastic energy  $f_{\text{elastic}}$ , the electrostatic energy  $f_{\text{electric}}$ , and the gradient energy  $f_{\text{grad}}$ . [Eq. 2]

$$F = \int_V [f_{\text{bulk}} + f_{\text{elastic}} + f_{\text{electric}} + f_{\text{grad}}] dV \quad (2)$$

In particular, the bulk free energy density  $f_{\text{bulk}}$  is expressed following the Landau theory. The bulk free energy density of Sm-PMN-PT is written as a 6-th order polynomial<sup>55</sup>

$$\begin{aligned} f_{\text{bulk}} = & \alpha_1 (P_x^2 + P_y^2 + P_z^2) + \alpha_{11} (P_x^4 + P_y^4 + P_z^4) + \alpha_{12} (P_x^2 P_y^2 + P_x^2 P_z^2 + P_y^2 P_z^2) \\ & + \alpha_{111} (P_x^6 + P_y^6 + P_z^6) + \alpha_{112} (P_x^2 (P_y^4 + P_z^4) + P_y^2 (P_x^4 + P_z^4) + P_z^2 (P_x^4 + P_y^4)) \\ & + \alpha_{123} P_x^2 P_y^2 P_z^2 \end{aligned} \quad (3)$$

where  $\alpha_i$ ,  $\alpha_{ij}$ ,  $\alpha_{ijk}$  are the Landau coefficients [Eq. 3]. The bulk free energy density of PVDF is expressed as [Eq. 4]

$$f_{\text{bulk}} = \alpha_1 P_x^2 + \alpha_2 P_y^2 + \alpha_3 P_z^2 + \alpha_{33} P_z^4 + \alpha_{333} P_z^6 \quad (4)$$

The expression is established following a uniaxial anisotropy with spontaneous polarization along the  $z$  axis (which is the PD during electrospinning), while polarization components along  $x$  and  $y$  axes assume paraelectric properties with higher order terms neglected.

Incorporation of MXene was considered through treating different background dielectric constants  $\epsilon_b$  by solving the electrostatic equilibrium equation<sup>56</sup>,

$$\nabla \cdot (\epsilon_0 \epsilon_b \mathbf{E} + \mathbf{P}) = 0 \quad (5)$$

where  $\epsilon_b$  correlated to MXene doping amount (Fig. 2f) to account for the variation of  $\beta$  phase fraction [Eq. 5].

The evolution of the domain structure was simulated for a single electrospun fiber under an applied electric field of  $1.2 \times 10^5\text{ V/m}$ ,

following the in-situ poling field (1.2 KV/cm) of electrospinning. The simulations were performed in a three-dimensional system with a total size of  $512\text{ nm} \times 512\text{ nm} \times 512\text{ nm}$  containing a single Sm-PMN-PT particle (diameter = 100 nm) in a PVDF matrix, which was then discretized into a three-dimensional array of  $128 \times 128 \times 128$  grids with a grid size of  $\Delta x = \Delta y = \Delta z = 4\text{ nm}$ . Periodic boundary conditions were employed for the polarization field, the electric field, and the mechanical displacement field. The material constants of Sm-PMN-PT and PVDF are listed in Supplementary Tables 2 and 3, respectively. All phase-field simulations in the present work were performed using the MuPRO Ferroelectric module for linux cluster software released from Mu-PRO LLC.

### Effective properties calculation of the piezoelectric composites

These simulations were performed using Mu-PRO Effective Properties module for linux cluster released from Mu-PRO LLC to systematically study and compare the stress transfer capability and electro-mechanical coupling effect of the electrospun nanofiber architecture with and without the MXene incorporation. The composite system consists of randomly oriented Sm-PMN-PT filler fibers with a diameter  $d = 200\text{ nm}$  at a total content of 3.23 vol% in a PVDF matrix. The total system size was taken as  $12.8\text{ }\mu\text{m} \times 12.8\text{ }\mu\text{m} \times 12.8\text{ }\mu\text{m}$ , which was discretized into a three-dimensional array of  $128 \times 128 \times 128$  grids. A three-dimensional periodic boundary condition was employed.

The effective dielectric constant  $\epsilon_r^{\text{eff}}$  and piezoelectric coefficient  $\mathbf{d}_r^{\text{eff}}$  of the composite system was calculated by modeling the coupled response of the electric displacement field  $\mathbf{D}(\mathbf{r})$  and the strain  $\boldsymbol{\epsilon}(\mathbf{r})$  of the composites to a small applied testing electric field  $\mathbf{E}_{\text{app}}$  under a stress-free condition. The material response was simulated by solving the electrostatic and elastic equilibrium equations coupled with linear constitutive relations<sup>5</sup>, i.e.,

$$\nabla \cdot \mathbf{D} = \nabla \cdot (\epsilon_0 \epsilon_r \mathbf{E} + \mathbf{d}\boldsymbol{\sigma}) = 0 \quad (6)$$

$$\nabla \cdot \boldsymbol{\sigma} = \nabla \cdot (\mathbf{c}\boldsymbol{\epsilon} - \mathbf{c}\mathbf{d}^T \mathbf{E}) = 0 \quad (7)$$

where  $\epsilon_0$  is the vacuum permittivity,  $\epsilon_r(\mathbf{r})$  is the relative dielectric constant of the local phase,  $\mathbf{c}(\mathbf{r})$  is the elastic stiffness, and  $\mathbf{d}(\mathbf{r})$  is the piezoelectric coefficient [Eqs. 6, 7]. A Fourier-spectral iterative-perturbation method<sup>57</sup> is employed for obtaining the numerical solution. The effective material properties of the composites were then calculated following  $\epsilon_0 \epsilon_r^{\text{eff}} \mathbf{E}_{\text{app}} = \langle \mathbf{D} \rangle$  and  $\mathbf{d}_r^{\text{eff}} \mathbf{E}_{\text{app}} = \langle \mathbf{d}\boldsymbol{\epsilon} \rangle$ , where  $\langle \mathbf{D} \rangle$  and  $\langle \mathbf{d}\boldsymbol{\epsilon} \rangle$  are the spatial average of the displacement response and the strain response with the whole system, respectively. The materials constants of the Sm-PMN-PT fillers and PVDF matrix are listed in Supplementary Note 2.

### Molecular dynamics (MD) calculation

In the MD simulations, 60 PVDF molecules with each 30 VDF monomers were constructed at 1 nm from the  $\text{Ti}_3\text{C}_2\text{T}_x$  nanosheets having an initial film density of  $1.3\text{ g/cm}^3$ . The periodic lattice of  $\text{Ti}_3\text{C}_2\text{T}_x$  nanosheets with OH or O surface terminations was directly taken from the literature<sup>58</sup> and was fixed at their lattice positions, interacting with the PVDF chains only via van der Waals and electrostatic interactions. The Universal Force Field (UFF)<sup>59</sup> was utilized to describe the intra- and intermolecular interactions for PVDF chains as well as the interaction between the PVDF and  $\text{Ti}_3\text{C}_2\text{T}_x$  nanosheets. The partial charges of the atoms of PVDF chains were assigned using the bond increments method, whereas the charges for the atoms of the  $\text{Ti}_3\text{C}_2\text{T}_x$  substrate were adopted from the first-principle calculations<sup>60</sup>. For equilibration, the PVDF- $\text{Ti}_3\text{C}_2\text{T}_x$  composite model was initially energy minimized with the energy and force convergences of  $1 \times 10^{-4}\text{ kcal mol}^{-1}$  and  $1 \times 10^{-6}\text{ kcal mol}^{-1}\text{ \AA}^{-1}$ , and then followed by a 2.5 ns run in the NVT ensemble. After that, an electrical field of 1.0 V/nm was applied to the

PVDF chains normal and opposite to the  $\text{Ti}_3\text{C}_2\text{T}_x$  substrate (i.e.,  $z$  direction) for another 2.0 ns, to investigate the polarization performance of the PVDF. The induced polarization was then calculated by summing the dipole moments of all the atoms of the PVDF film within the film volume  $V$  as [Eq. 8]

$$\mathbf{P} = \frac{1}{V} \sum_i \mathbf{u}_i = \frac{1}{V} \sum_i q_i \mathbf{r}_i \quad (8)$$

where  $q_i$  and  $\mathbf{r}_i$  are the particle charge and Cartesian coordinate vector of the  $i$ th atom of the PVDF. In addition, the interaction strength between one single PVDF chain and the  $\text{Ti}_3\text{C}_2\text{T}_x$  substrate was estimated by applying a constant force along the  $z$  direction to each atom of the PVDF chain. A series of MD simulations were performed with varying forces using an incremental step of 0.01 or 0.002 kcal mol<sup>-1</sup>Å<sup>-1</sup> to produce the minimum pulling force required for fully desorbing the PVDF chain away from the  $\text{Ti}_3\text{C}_2\text{T}_x$  substrate. For all the simulations, the temperature was maintained at 300 K using the Noé-Hoover thermostat with a relaxation time of 1.0 ps. Newton's equations of motion were integrated using the velocity-Verlet algorithm with a time step of 1.0 fs and periodic boundary conditions were applied in all three dimensions. The non-bonded van der Waals interactions were cut off at 10 Å and the long-range electrostatic interactions were calculated using the particle-particle particle-mesh solver<sup>61</sup> with  $5 \times 10^{-6}$  accuracy tolerance. All the MD simulations were carried out using the Large-scale Atomic/Molecular Massively Parallel Simulator software<sup>62</sup>.

## Data availability

The data that supports the findings of this study are available from the authors on reasonable request.

## Code availability

The code that supports the findings of this study is available from the authors on reasonable request.

## References

- Qiu, C. et al. Transparent ferroelectric crystals with ultrahigh piezoelectricity. *Nature* **577**, 350–354 (2020).
- Li, F. et al. Ultrahigh piezoelectricity in ferroelectric ceramics by design. *Nat. Mater.* **17**, 349–354 (2018).
- Li, F. et al. Giant piezoelectricity of Sm-doped Pb ( $\text{Mg}_{1/3}\text{Nb}_{2/3}$ )  $\text{O}_3$ - $\text{PbTiO}_3$  single crystals. *Science* **364**, 264–268 (2019).
- Chen, G., Li, Y., Bick, M. & Chen, J. Smart textiles for electricity generation. *Chem. Rev.* **120**, 3668–3720 (2020).
- Su, Y. et al. Muscle fibers inspired high-performance piezoelectric textiles for wearable physiological monitoring. *Adv. Funct. Mater.* **31**, 2010962 (2021).
- Deng, W. et al. Piezoelectric nanogenerators for personalized healthcare. *Chem. Soc. Rev.* **51**, 3380–3435 (2022).
- Zhao, X., Askari, H. & Chen, J. Nanogenerators for smart cities in the era of 5G and Internet of Things. *Joule* **5**, 1391–1431 (2021).
- Liu, Y. et al. Ferroelectric polymers exhibiting behaviour reminiscent of a morphotropic phase boundary. *Nature* **562**, 96–100 (2018).
- Meng, N. et al. Ultrahigh  $\beta$ -phase content poly(vinylidene fluoride) with relaxor-like ferroelectricity for high energy density capacitors. *Nat. Commun.* **10**, 4535 (2019).
- Krishnamoorthy, K. et al. Probing the energy conversion process in piezoelectric-driven electrochemical self-charging supercapacitor power cell using piezoelectrochemical spectroscopy. *Nat. Commun.* **11**, 2351 (2020).
- Liu, Y. et al. Chirality-induced relaxor properties in ferroelectric polymers. *Nat. Mat.* **19**, 1169–1174 (2020).
- Chen, C. et al. A method for quantitatively separating the piezoelectric component from the as-received “Piezoelectric” signal. *Nat. Commun.* **13**, 1391 (2020).
- Su, Y. et al. Piezoelectric fiber composites with polydopamine interfacial layer for self-powered wearable biomonitoring. *Nano Energy* **89**, 106321 (2021).
- Lovinger, A. J. Ferroelectric polymers. *Science* **220**, 1115–1121 (1983).
- Sencadas, V., Gregorio, R. Jr & Lanceros-Méndez, S.  $\alpha$  to  $\beta$  phase transformation and microstructural changes of PVDF films induced by uniaxial stretch. *J. Macromol. Sci.* **48**, 514–525 (2009).
- Park, C., Ounaies, Z., Wise, K. E. & Harrison, J. S. In situ poling and imidization of amorphous piezoelectric polyimides. *Polymer* **45**, 5417–5425 (2004).
- Ren, J. et al. Enhanced Dielectric and Ferroelectric Properties of Poly(vinylidene fluoride) through Annealing Oriented Crystallites under High Pressure. *Macromolecules* **55**, 2014–2027 (2022).
- Zhang, Y. et al. Ferroelectret materials and devices for energy harvesting applications. *Nano Energy* **57**, 118–140 (2019).
- Park, J. et al. Ferroelectric Polymer Nanofibers Reminiscent of Morphotropic Phase Boundary Behavior for Improved Piezoelectric Energy Harvesting. *Small* **18**, 2104472 (2022).
- Liu, Y. et al. Insights into the morphotropic phase boundary in ferroelectric polymers from the molecular perspective. *J. Phys. Chem. C* **123**, 8727–8730 (2019).
- Han, M. et al. Three-dimensional piezoelectric polymer microsystems for vibrational energy harvesting, robotic interfaces and biomedical implants. *Nat. Electron.* **2**, 26–35 (2019).
- Libanori, A., Chen, G., Zhao, X., Zhou, Y. & Chen, J. Smart textiles for personalized healthcare. *Nat. Electron.* **5**, 142–156 (2022).
- Chen, G. et al. Electronic textiles for wearable point-of-care systems. *Chem. Rev.* **122**, 3259–3291 (2022).
- Qin, Y., Wang, X. & Wang, Z. L. Microfibre-nanowire hybrid structure for energy scavenging. *Nature* **451**, 809–813 (2008).
- Su, Y. et al. Self-powered respiration monitoring enabled by a triboelectric nanogenerator. *Adv. Mater.* **33**, 2101262 (2021).
- Yan, C. et al. Epidermis-inspired ultrathin 3D cellular sensor array for self-powered biomedical monitoring. *ACS Appl. Mater. Interfaces* **10**, 41070–41075 (2018).
- Wei, Q. et al. MXene-sponge based high-performance piezoresistive sensor for wearable biomonitoring and real-time tactile sensing. *Small Methods* **6**, 2101051 (2022).
- Shen, Z. H. et al. Phase-field modeling and machine learning of electric-thermal-mechanical breakdown of polymer-based dielectrics. *Nat. Commun.* **10**, 1843 (2019).
- Shen, Z. H. et al. High-throughput phase-field design of high-energy-density polymer nanocomposites. *Adv. Mater.* **30**, 1704380 (2018).
- Shen, Z. H. et al. Designing polymer nanocomposites with high energy density using machine learning. *npj Comput. Mater.* **7**, 110 (2021).
- Peng, S. et al. Direct Detection of Local Electric Polarization in the Interfacial Region in Ferroelectric Polymer Nanocomposites. *Adv. Mater.* **31**, 1807722 (2019).
- Shvartsman, V. V., Kiselev, D. A., Solnyshkin, A. V., Lupascu, D. C. & Silibin, M. V. Evolution of poled state in P(VDF-TrFE)/(Pb,Ba)(Zr,Ti) $\text{O}_3$  composites probed by temperature dependent piezoresponse and kelvin probe force microscopy. *Sci. Rep.* **8**, 378 (2018).
- Chen, Q., Shen, Y., Zhang, S. & Zhang, Q. M. Polymer-based dielectrics with high energy storage density. *Annu. Rev. Mater. Sci.* **45**, 433–458 (2015).
- Wu, C. M. & Chou, M. H. Polymorphism, piezoelectricity and sound absorption of electrospun PVDF membranes with and without carbon nanotubes. *Compos. Sci. Technol.* **127**, 127–133 (2016).

35. Cheon, S. et al. High-Performance Triboelectric Nanogenerators Based on Electrospun Polyvinylidene Fluoride–Silver Nanowire Composite Nanofibers. *Adv. Funct. Mater.* **28**, 1703778 (2018).
36. Martins, P. et al. Linear anhysteretic direct magnetoelectric effect in  $\text{Ni}_{0.5}\text{Zn}_{0.5}\text{Fe}_2\text{O}_4$ /poly(vinylidene fluoride-trifluoroethylene) 0-3 nanocomposites. *J. Phys. D: Appl. Phys.* **44**, 482001 (2011).
37. Martins, P., Costa, C. M., Ferreira, J. C. C. & Lanceros-Mendez, S. Correlation between Crystallization Kinetics and Electroactive Polymer Phase Nucleation in Ferrite/Poly(vinylidene fluoride) Magnetoelectric Nanocomposites. *J. Phys. Chem. B* **116**, 794–801 (2012).
38. Martins, P., Costa, C. M., Benelmekki, M., Botelho, G. & Lanceros-Mendez, S. On the origin of the electroactive poly(vinylidene fluoride) b-phase nucleation by ferrite nanoparticles via surface electrostatic interactions. *Cryst. Eng. Comm.* **14**, 2807–2811 (2012).
39. Thakur, P., Kool, A., Bagchi, B., Das, S. & Nandy, P. Effect of in situ synthesized  $\text{Fe}_2\text{O}_3$  and  $\text{Co}_3\text{O}_4$  nanoparticles on electroactive  $\beta$ -phase crystallization and dielectric properties of poly(vinylidene fluoride) thin films. *Phys. Chem. Chem. Phys.* **17**, 1368–1378 (2015).
40. Bhunia, R. et al. Milli-watt power harvesting from dual triboelectric and piezoelectric effects of multifunctional green and robust reduced graphene oxide/P(VDF-TrFE) composite flexible films. *ACS Appl. Mater. Interfaces* **11**, 38177–38189 (2019).
41. Pusty, M., Sinha, L. & Shirage, P. M. A flexible self-poled piezoelectric nanogenerator based on a rGO–Ag/PVDF nanocomposite. *N. J. Chem.* **43**, 284–294 (2019).
42. Abolhasani, M. M., Shirvanimoghaddam, K. & Naebe, M. PVDF/graphene composite nanofibers with enhanced piezoelectric performance for development of robust nanogenerators. *Compos. Sci. Technol.* **138**, 49–56 (2017).
43. Li, T. et al. High-performance poly(vinylidene difluoride)/dopamine core/shell piezoelectric nanofiber and its application for biomedical sensors. *Adv. Mater.* **33**, 2006093 (2021).
44. Kongklang, T. et al. Electrospun polyoxymethylene: spinning conditions and its consequent nanoporous nanofiber. *Macromolecules* **41**, 4746–4752 (2008).
45. Feng, Y. et al. An ultrahigh discharged energy density achieved in an inhomogeneous PVDF dielectric composite filled with 2D MXene nanosheets via interface engineering. *J. Mater. Chem. C* **6**, 13283–13292 (2018).
46. VahidMohammadi, A., Rosen, J. & Gogotsi, Y. The world of two-dimensional carbides and nitrides (MXenes). *Science* **372**, 6547 (2021).
47. Tu, S., Jiang, Q., Zhang, X. & Alshareef, H. N. Large dielectric constant enhancement in MXene percolative polymer composites. *ACS Nano* **12**, 3369–3377 (2018).
48. Liu, Z. et al. Piezoelectric-effect-enhanced full-spectrum photoelectrocatalysis in p-n heterojunction. *Adv. Funct. Mater.* **29**, 1807279 (2019).
49. Niu, X. et al. High-performance PZT-based stretchable piezoelectric nanogenerator. *ACS Sustain. Chem. Eng.* **7**, 979–985 (2018).
50. Li, J. et al. Hydrogen bond interaction promotes flash energy transport at MXene-solvent interface. *J. Phys. Chem. C* **124**, 10306–10314 (2020).
51. Gu, L. et al. Enhancing the current density of a piezoelectric nanogenerator using a three-dimensional intercalation electrode. *Nat. Commun.* **11**, 1030 (2020).
52. Marwat, M. A. et al. Ultrahigh energy density and thermal stability in sandwich-structured nanocomposites with dopamine@Ag@BaTiO<sub>3</sub>. *Energy Storage Mater.* **31**, 492–504 (2020).
53. Ahmed, A. et al. Triboelectric Nanogenerator versus Piezoelectric Generator at Low Frequency (<4 Hz): A Quantitative Comparison. *iScience* **23**, 101286 (2020).
54. Chen, L. Q. Phase-field method of phase transitions/domain structures in ferroelectric thin films: a review. *J. Am. Ceram. Soc.* **91**, 1835–1844 (2008).
55. Khakpash, N. et al. Misfit strain phase diagrams of epitaxial PMN–PT films. *Appl. Phys. Lett.* **106**, 082905 (2015).
56. Tagantsev, A. K. Landau Expansion for Ferroelectrics: Which Variable to Use? *Ferroelectrics* **375**, 19–27 (2008).
57. Hu, S. Y. & Chen, L. Q. A phase-field model for evolving microstructures with strong elastic inhomogeneity. *Acta. Mater.* **49**, 1879–1890 (2001).
58. Hu, T. et al. Vibrational properties of  $\text{Ti}_3\text{C}_2$  and  $\text{Ti}_3\text{C}_2\text{T}_2$  (T = O, F, OH) monosheets by first-principles calculations: a comparative study. *Phys. Chem. Chem. Phys.* **17**, 9997–10003 (2015).
59. Rappé, A. K., Casewit, C. J., Colwell, K. S., Goddard, W. A. III & Skiff, W. M. UFF, a full periodic table force field for molecular mechanics and molecular dynamics simulations. *J. Am. Chem. Soc.* **114**, 10024–10035 (1992).
60. Berdiyrov, G. R., Madjet, M. E. & Mahmoud, K. A. Ionic sieving through  $\text{Ti}_3\text{C}_2(\text{OH})_2$  MXene: first-principles calculations. *Appl. Phys. Lett.* **108**, 113110 (2016).
61. Hockney, R. W. & Eastwood, J. W. *Computer Simulation Using Particles* (CRC Press, New York, 1988).
62. Plimpton, S. Fast parallel algorithms for short-range molecular dynamics. *J. Comput. Phys.* **117**, 1–19 (1995).

## Acknowledgements

Y.S. acknowledges the National Natural Science Foundation of China (Grant No. 62074027). J.C. acknowledges the Henry Samueli School of Engineering & Applied Science and the Department of Bioengineering at University of California, Los Angeles for the startup support. X.C., T.Y., and L.-Q.C. acknowledge supports from the U.S. Department of Energy, Office of Basic Energy Sciences, under Award No. DE-SC0020145.

## Author contributions

Y.S., J.C., and F.L. planned the study and guided the whole project. Y.S., W.L., C.C., and H.P. organized the data and draw the figures. Y.S., J.C., W.L., S.Y., X.Zhao, X.X., G.X., H.T., and Y.J. performed the data analysis and guided the experiment. Y.S., J.C., Y.Z., G.C., and F.L. wrote the paper. Y.S., W.L., X.C., T.Y., and L.C. performed the phase-field simulation. X.Zhang and B.L. performed the molecular dynamics calculation. All authors commented and edited the paper. J.C. submitted the paper and was the lead contact.

## Competing interests

The authors declare no competing interests.

## Additional information

**Supplementary information** The online version contains supplementary material available at <https://doi.org/10.1038/s41467-022-32518-3>.

**Correspondence** and requests for materials should be addressed to Tiannan Yang, Bei Li, Fei Li or Jun Chen.

**Peer review information** *Nature Communications* thanks Pedro Martins, Kwi-Il Park and the other anonymous reviewer(s) for their contribution to the peer review of this work.

**Reprints and permission information** is available at <http://www.nature.com/reprints>

**Publisher's note** Springer Nature remains neutral with regard to jurisdictional claims in published maps and institutional affiliations.

**Open Access** This article is licensed under a Creative Commons Attribution 4.0 International License, which permits use, sharing, adaptation, distribution and reproduction in any medium or format, as long as you give appropriate credit to the original author(s) and the source, provide a link to the Creative Commons license, and indicate if changes were made. The images or other third party material in this article are included in the article's Creative Commons license, unless indicated otherwise in a credit line to the material. If material is not included in the article's Creative Commons license and your intended use is not permitted by statutory regulation or exceeds the permitted use, you will need to obtain permission directly from the copyright holder. To view a copy of this license, visit <http://creativecommons.org/licenses/by/4.0/>.

© The Author(s) 2022